Title
LEED THEORY FOR INCOMMENSURATE OVERLAYERS: APPLICATION TO GRAPHITE ON Pt(111)

Author
Hu, Z.P.

Publication Date
1986-06-01

Lawrence Berkeley Laboratory
UNIVERSITY OF CALIFORNIA

Materials & Molecular Research Division

Submitted to Surface Science

LEED THEORY FOR INCOMMENSURATE OVERLAYERS: APPLICATION TO GRAPHITE ON Pt(111)

Z.-P. Hu, D.F. Ogletree, M.A. Van Hove,
and G.A. Somorjai

June 1986

Prepared for the U.S. Department of Energy under Contract DE-AC03-76SF00098

DISCLAIMER

LBL-21511

LEED THEORY FOR INCOMMENSURATE OVERLAYERS: APPLICATION TO GRAPHITE ON Pt(111)

Hu Zi-pu*, D.F. Ogletree, M.A. Van Hove and G.A. Somorjai

Materials and Molecular Research Division
Lawrence Berkeley Laboratory, and
University of California
Berkeley, CA 94720

Submitted to Surface Science
June, 1986

---

*Permanent address: Physics Department, The University of Science and Technology of China, Hefei, Anhui, People's Republic of China.

ABSTRACT

A dynamical LEED analysis is applied to study the structure of incommensurate overlayers. The previously described Beam Set Neglect method is extended to the incommensurate case, providing an efficient theoretical scheme for calculating the required LEED beam intensities.

This method is used to investigate the structure of an incommensurate graphite overlayer on the Pt(111) surface by analyzing the specular diffraction beam intensities at various angles. The measured LEED intensities are well represented by a surface model consisting of a graphite layer 3.70±0.05 Å above the Pt(111) surface, supported by at least a partial layer of "intercalated" carbidic carbon atoms chemisorbed in three-fold hollow sites 1.25±0.10 Å above the Pt(111) surface. A "data subdivision method" is applied in the R-factor analysis to distinguish between the different R-factor minima.

1. Introduction

Ordered monolayers of adsorbates on solid surfaces often form incommensurate structures, in the sense that an overlayer exists with a lattice which is not simply related to the lattice of the substrate which supports it. This lack of a simple relationship expresses itself as an irrational ratio of lattice constants and/or a misalignment of the overlayer and substrate lattices.[1] In an incommensurate system the adsorbed atoms or molecules occupy many different positions, or sites, relative to the substrate atoms.

While structure analysis of commensurate surface structures using low energy electron diffraction (LEED) beam intensities and a dynamical LEED theory is well advanced, the analysis of incommensurate surface structures is not. The purpose of this paper is to develop a dynamical LEED theory for the study of the structure of incommensurate surface structures. This theory is then applied to solve the structure of an incommensurate graphite overlayer on the platinum (111) single crystal surface. We find an unexpected bonding geometry; an unusually large 3.70 Å platinum-carbon layer separation. This is explained by the presence of a layer of intercalated chemisorbed carbon layer atoms located between the metal and the graphite layers. The layer separation between the intercalated carbon and the graphite is intermediate between what is expected for strong covalent and weak Van der Waals bonding.

2. Incommensurate Structures

Incommensurate overlayers are very common for rare gas atoms and small molecules physisorbed on the graphite (0001) basal plane[2-6] and on metal surfaces.[2,7-16] Incommensurate alkali metal overlayers have also been observed on the graphite basal plane.[17,18] Many of these incommensurate structures involve a close packed overlayer where the overlayer lattice is determined by the adsorbate density, hence it is often out of registry with the substrate lattice. There are also examples of incommensurate metal overlayers on metal substrates,[3,19,20] including the case of some clean metal reconstructions.[21]

There is another class of incommensurate systems where the overlayer has a well-defined geometry, which is not much influenced by the substrate geometry. Such systems include graphitized carbon layers on various metals[22-26] and compound layers (e.g. oxides) grown on metal surfaces.[27-35]

In incommensurate overlayer systems, the interaction energy between overlayer atoms or molecules is generally strong compared to the variation in the substrate-overlayer interaction energy across the surface. For example, the corrugation of the Van der Waals potential on the basal plane of graphite is quite small, hence the large number of observations of incommensurate physisorbed overlayers reported for graphite substrates.[3]

The presence of incommensurate overlayers is deduced from diffraction experiments, including low energy electron diffraction (LEED) and x-ray diffraction; the major features of the diffraction pattern can be explained as the superposition of two independent diffraction patterns, one due to the substrate alone and one due to the overlayer alone. Additional weak beams due to either multiple scattering in LEED or substrate-induced buckling of the overlayer may also be visible in the diffraction pattern.

The overlayer diffraction pattern yields the (average) lattice constant of the overlayer. This lattice constant may be sufficient to recognize the overlayer; for example, the diffraction rings of "graphitic" carbon on platinum correspond to a lattice constant within ½% of that of the basal plane of bulk graphite. The diffraction pattern also shows the relative angular orientation of the substrate and overlayer lattices. In some cases there may be many randomly oriented overlayer domains; then the superposition of sharp diffraction beams from different domains produces a ring-like diffraction pattern centered on the specular beam. If multiple scattering is strong enough, similar ring-like patterns centered on the other substrate beams will also be visible in the diffraction pattern.

To get additional structural information on incommensurate layers the beam intensities must be investigated. In this way the overlayer-substrate spacing, the internal structure of the overlayer (if there is more than one atom in the overlayer unit cell), and the

substrate structure may be investigated. A substrate-induced overlayer buckling, due to the registry mismatch will also be reflected in LEED beam intensities, especially in the extra (overlayer-induced) beams.

There are few techniques other than x-ray and electron diffraction that can study the structure of incommensurate overlayers. Fine structure techniques such as surface extended x-ray absorption fine structure (SEXAFS),[36] angle-resolved photoelectron emission fine structure (ARPEFS),[37] extended appearance potential fine structure (EAPFS),[38] and surface extended energy loss fine structure (SEELFS)[39,40] can potentially probe the internal structure of the overlayer. However, fine structure techniques cannot easily determine the overlayer-substrate spacing, because of the distribution of overlayer-substrate atom distances and directions resulting from the incommensurate relation between overlayer and substrate.

A theory is required to extract structural information on incommensurate systems from LEED intensities. A kinematic LEED theory was developed by Cohen et al.[12] The distance between overlayer and substrate is determined through a Fourier transformation of the ratio of the specular-beam intensity of the overlayer-covered surface to that of the specular-beam intensity of the clean surface. Constant momentum transfer averaging is used to emphasize the kinematic features of this approximation. This theory has been successfully applied to incommensurate overlayers of Xe on Ag (111)[12] and of Ar and Kr on graphite.[5,6] A dynamical LEED theory, incorporating multiple scattering, was developed by Stoner et al.[14] It was also applied to the Xe on

Ag (111) system and confirmed the structural results of Cohen et al.:[12] a Xe overlayer 3.5±0.1 Å above the Ag substrate. This dynamical theory is computationally rather cumbersome, as we shall discuss in Section 3.

Carbonaceous layers on metal surfaces are known to play an important role in catalytic reactions and other surface processes, such as lubrication.[41] Nevertheless, very little is known about the structure and bonding of these layers, which include chemisorbed carbon overlayers, graphite overlayers, and metal-carbide compound phases. Such layers may be disordered or ordered, and in the latter case they may be commensurate or incommensurate. Of such systems, only three have been structurally studied to our knowledge: Ni(110)-graphite (incommensurate),[40] Ni(111)-(1x1)-graphite (commensurate),[39] and Ni(100)-p(2x2)-2C.[42]

Carbon is adsorbed on transition metal surfaces in three basic forms, distinguished by different chemical environments: as part of a chemisorbed molecule, as "carbidic" carbon, and as "graphitic" carbon. The bonding of the carbon atoms affects the fine structure of the carbon KVV Auger transitions. This has been used as a fingerprint for the different types of surface carbon. Carbon chemisorbed in the carbidic form has an Auger lineshape similar to that of bulk metal-carbides, and the chemisorbed graphitic form has a lineshape similar to bulk graphite.[43] The Auger lineshape has also been used to distinguish between carbon in intact chemisorbed molecules and residual surface carbon due to molecular decomposition; an example is intact and decomposed carbon monoxide on transition metal surfaces.[44]

Platinum is widely used in pure form and in combination with other materials for hydrocarbon catalysis. Experiment has shown that under catalytic conditions there is a significant amount of carbon chemisorbed on the metal surface.[45] In this work we explore the structure of one phase of carbon on the platinum (111) surface, the incommensurate graphitic phase.

The separation between the graphite layer and the platinum surface was found to be 3.70±0.05 Å, substantially larger than expected from known atomic radii, and also large compared to the 2.80±0.08 Å separation found for the commensurate graphite layer on Ni (111).[43] We show that this large separation can be explained by the presence of additional carbon atoms chemisorbed in three-fold hollow sites 1.25±0.10 Å above the Pt(111) surface.

3. Theory

We shall treat the idealized case of a strictly incommensurate overlayer: no large coincidence unit cell, no domain boundaries and no buckling of overlayer or substrate. The overlayer may contain any number of atoms in its unit cell, such as 2 atoms for a graphite layer or N atoms for a film of N simple atomic layers, a molecular layer or a compound layer.

3.1 Beam categories

Under these conditions, an incident plane wave representing an electron beam can diffract into various beams which we classify as follows, see Fig. 1.

1. The specular beam, labeled $\vec{0}$. Even in the kinematic limit, both the overlayer and the substrate contribute to the diffracted specular beam, yielding coherent interference.

2. The "substrate beams", labeled $\vec{G}$, where $\{\vec{G}\}$ is the set of 2-dimensional reciprocal lattice vectors of the substrate. These beams are present for the clean substrate and for the overlayer covered surface. In the kinematic limit such as in X-ray diffraction, they are generated by the substrate alone, with no contribution from the overlayer.

3. The "overlayer beams", labeled $\vec{g}$, where $\{\vec{g}\}$ is the set of 2-dimensional reciprocal lattice vectors of the overlayer. These beams exist only in the presence of the overlayer. In the kinematic limit they receive no contribution from the substrate. With the exception of the specular beam $\vec{g}=\vec{G}=\vec{0}$, the inequality $\vec{g}\neq\vec{G}$ holds for all $\vec{g}$ and $\vec{G}$, because of the incommensurability. With overlayer domains randomly oriented on the substrate, the overlayer beams produce rings around the specular beam.

4. The "combination beams", labeled $\vec{g}+\vec{G}$, where $\vec{G}$ and $\vec{g}$ have been defined above, see Fig. 1. These are beams induced by multiple scattering involving at least one non-specular diffraction by the substrate and at least one non-specular diffraction by the overlayer. In the kinematic limit, e.g. in X-ray diffraction, the combination beams do not exist, since at least double scattering is needed to generate them. Higher than double scattering does not produce more beams: for instance, the triply-scattered beam $\vec{g}_1+\vec{g}_2+\vec{G}$ can be labeled $\vec{g}+\vec{G}$

(with $\vec{g}=\vec{g}_1+\vec{g}_2$), which already exists in double scattering. In general, any point in the 2-dimensional reciprocal space can be reached by a suitable combination $\vec{g}+\vec{G}$, i.e. any position on the LEED screen can be reached by electrons diffracted by an incommensurate surface.[46] However, most of those positions require that either $|\vec{g}|$ or $|\vec{G}|$ be large, for simple geometrical reasons. An evanescent wave is then implicated,[47] which carries very little current from layer to layer and yields a negligible measured intensity. Thus, only a finite set of combinations $\{\vec{g}+\vec{G}\}$ produces intense spots on a LEED screen, namely those that correspond to relatively small $|\vec{g}|$ and $|\vec{G}|$. In the case of random overlayer orientations, rings with radii proportional to $|\vec{g}|$ are produced around <u>each</u> beam $\vec{G}$, not only around the specular beam.

3.2 <u>The Need for an Approximation</u>

The difficulty of dynamical LEED theory for incommensurate layers is the profusion of beams $\vec{g}+\vec{G}$ that have to be included to accurately calculate beam intensities: the required number of beams grows without bound as the desired accuracy increases. The worst aspect of this profusion of beams is that the diffraction properties of all surface layers must be calculated for the many beam directions involved.[14] It is therefore necessary to approximate the process in the incommensurate case. A useful approach to the calculation of LEED intensities for incommensurate surfaces has been described in Ref. 14. The possible scattering paths are classified by the number of scatterings involved, not counting zero-angle forward scattering (which is strong and cannot be used as a perturbation in an expansion). Fig. 2 illustrates this classification for up to 4 scatterings for the four types of beams

defined above. In Ref. 14 many of the terms of Fig. 2 were explicitly calculated. The higher the number of scatterings involved, the higher was the number of matrix elements for layer diffraction between different beams that must be computed. This requires a large computational effort. It was, however, noticed in calculations for an incommensurate xenon layer on Ag(111) that third- and higher-order multiple scattering (as defined below) gave only small contributions to the beam intensities.

We must define here what we mean by matrix elements for layer diffraction. These are the conventional[47] plane-wave diffraction amplitudes $M^{\pm\,\pm}_{\vec{g}',\vec{g}}$ for an incident plane wave $\vec{g}^{\pm}$ scattering into an exiting plane wave $\vec{g}'^{\pm}$ (+/- indicate propagation towards/from the substrate, i.e. into/out of the surface). In the commensurate case, the linear momenta $\vec{k}^{\pm}_{g}$ of the beams are conveniently referred to the monentum $\vec{k}_0$ of the incident beam:

$$\vec{k}^{\pm}_{g} = (k_{ox} + g_x,\ k_{oy} + g_y,\ \pm\{2E - [k_{ox} + g_x]^2 - [k_{oy} + g_y]^2\}^{1/2}).$$

using atomic units and a z-axis perpendicular to the surface. This is because multiple scattering within a commensurate layer can be efficiently treated simultaneously for all reciprocal lattice vectors $\vec{g}$ of that layer. With incommensurate surfaces, referring back to $\vec{k}_0$ is often no longer useful. For instance, an incommensurate overlayer finds itself exposed to a beam $\vec{G}^{-}$ due to reflection of the incident beam $\vec{0}$ by the substrate. Since $\vec{G}^{-}$ belongs to the <u>substrate</u> reciprocal lattice and not to the overlayer reciprocal lattice, the overlayer diffraction of beam $\vec{G}^{-}$ cannot be efficiently calculated at the same time as the matrix

elements $M^{\pm\pm}_{\vec{g},\vec{g}}$ for diffraction from overlayer beam $\vec{g}^{\pm}$ to $\vec{g}'^{\pm}$ by the overlayer. It is as if the overlayer were receiving a totally new incident beam unrelated to the original beam $\vec{k}_o$.

We therefore need to expand our notation and use $M^{\pm\pm}_{\vec{g},\vec{g}}(\vec{G})$ to denote the diffraction by the overlayer of a beam $(\vec{G}+\vec{g})^{\pm}$ into a beam $(\vec{G}+\vec{g}')^{\pm}$, where $\vec{g}$ and $\vec{g}'$ belong to the overlayer reciprocal lattice and $\vec{G}$ belongs to the substrate reciprocal lattice. Conversely, we also need matrix elements $M^{\pm\pm}_{\vec{G},\vec{G}}(\vec{g})$ to denote the diffraction by a substrate layer of a beam $(\vec{g}+\vec{G})^{\pm}$ into a beam $(\vec{g}+\vec{G}')^{\pm}$.

These matrix elements are meant to contain all multiple scattering <u>within</u> the layers under consideration, i.e. they should be exact. (But approximations to intralayer multiple scattering may of course be introduced).[48] In fact, as implied by Fig. 2, we shall consider the entire substrate as a single, very thick layer: we then need only calculate the reflection matrix elements $M^{\pm\pm}_{\vec{G},\vec{G}}(\vec{g}) = R_{\vec{G},\vec{G}}(\vec{g})$, which can be obtained, for instance, by repeating the conventional layer doubling calculation in the substrate for each "independent" incident direction $\vec{g}^{+}$. Thus, when we count multiple scattering events, as in Fig. 2, we do not count any multiple scattering that occurs within the overlayer or any multiple scattering that occurs within the substrate. Instead we count only changes in direction as they appear in diagrams of the type shown in Fig. 2. Note the exclusion of (zero-angle) forward scattering, since it cannot be considered weak in a perturbation treatment of multiple scattering.

3.3 Beam Set Neglect

We now recall the principle of the Beam Set Neglect method, which was developed[49] to deal with a different but related problem in LEED: in the presence of overlayers with large commensurate unit cells on substrates with small unit cells, the number of beams can also be very large compared to the uncovered substrate.

If we limit ourselves to second-order multiple scattering events, we find that many beams do not contribute to the intensities of the other beams and therefore can be ignored. Specifically, to calculate the intensity of any particular exiting beam $\vec{g}$ due to the incident beam $\vec{0}$, it is sufficient to include only the two beam sets $\{\vec{G}\}$ and $\vec{g}+\{\vec{G}\}$, where $\{\vec{G}\}$ again represents all reciprocal lattice vectors of the substrate surface. One thereby obtains the intensity not only of $\vec{g}$ but of all exiting beams $\vec{g}+\{\vec{G}\}$ and $\{\vec{G}\}$. Compared to the case of the uncovered surface, the number of beams in the calculation has only been doubled, rather than being multiplied in proportion to the unit cell size: this yields considerable savings in computational effort, since the latter can scale as the square or cube of the number of beams. To calculate the intensity of a different beam $\vec{g}'$ which does not belong to the sets $\{\vec{G}\}$ and $\vec{g}+\{\vec{G}\}$, the same scheme is repeated with the beam sets $\{\vec{G}\}$ and $\vec{g}'+\{\vec{G}\}$, etc.

We now apply this "Beam Set Neglect" approach to the incommensurate case. Again two beam sets are defined as $\{\vec{G}\}$ and $\vec{g}+\{\vec{G}\}$ to calculate the intensity of a particular beam $\vec{g}$. (If one wishes to calculate the

intensity of the specular beam $\vec{0}$ or of a substrate beam $\vec{G}$, it is sufficient to use the single set $\{\vec{G}\}$, as it is in the commensurate case.[47] This is because the two beam sets collapse into each other in those cases.) It is easily seen that this choice of beam sets allows inclusion of all scattering paths shown in Fig. 2 in the columns for single and double scattering. Thus again the Beam Set Neglect approach eliminates only third-and higher-order terms. The calculations of Ref. 21 support the validity of this approach at least for Xe on Ag(111), by showing that higher-order terms provide only small corrections.

A convenient implementation of this method uses Renomalized Forward Scattering (RFS) or Layer Doubling (LD) to calculate the intensities from the layer diffraction matrices.[47] Because RFS can easily be iterated to convergence, and because LD is inherently self-consistent, many higher-order multiple scattering paths can be efficiently included after all: these show up in the scheme of Fig. 2 in columns corresponding to higher-order scattering. But these are only paths that involve the beams of the two included beam sets. Paths that involve beams which do not belong to these two sets are still ignored.

To illustrate the convenience of the BSN method for incommensurate overlayers, we list the diffraction matrix elements that are needed to calculate the intensities of the various types of beams.

For convenience, we first summarize the definitions of matrix elements given in Section 3.2:

$R^{-,+}_{\vec{G}',\vec{G}}(\vec{g})$ = substrate reflection from beam $(\vec{g}+\vec{G})^+$ to beam $(\vec{g}+\vec{G}')^-$, including all orders of multiple scattering within the substrate;

$M^{\pm,\pm}_{\vec{g}',\vec{g}}(\vec{G})$ = overlayer reflection from beam $(\vec{G}+\vec{g})^\pm$ to beam $(\vec{G}+\vec{g}')^\pm$, including all multiple scattering within the overlayer.

Here $\{\vec{g}\}$ = overlayer beams, $\{\vec{G}\}$ = substrate beams, +(-) = inward (outward) propagation.

1. The specular $(\vec{0})$ beam requires the knowledge of $R^{+,+}_{00}(\vec{0})$ for the substrate taken as a whole, and of $M^{\alpha\beta}_{00}(0)$ with $(\alpha\beta)$ = (-+), (++) and (--) for the overlayer. It is trivial to also generate the case $(\alpha\beta)$ = (+-) at the same time. This allows the inclusion of multiple back-and-forth scattering between overlayer and substrate in Renormalized Forward Scattering or Layer Doubling, going beyond the minimal BSN method with negligible extra computational cost.

2. To obtain a $\vec{G}$-beam intensity $(\vec{G}\neq\vec{0})$, one needs $R^{+,+}_{G0}(\vec{0})$, $M^{++}_{00}(\vec{0})$ and $M^{--}_{00}(\vec{0})$. One easily obtains also $R^{+,+}_{00}(\vec{0})$, $R^{+,+}_{0G}(\vec{0})$, $R^{+,+}_{GG}(\vec{0})$, $M^{+-}_{00}(\vec{0})$ and $M^{+-}_{00}(\vec{G})$ at the same time, which provides access to a number of higher-order terms. But for a different beam $\vec{G}'\neq\vec{G}$, a new calculation is required.

3. To calculate a $\vec{g}$-beam intensity $(\vec{g}\neq\vec{0})$, one requires $R^{+,+}_{00}(\vec{0})$, $R^{+,+}_{00}(\vec{g})$, $M^{++}_{00}(\vec{0})$, $M^{++}_{g0}(\vec{0})$, $M^{-+}_{g0}(\vec{0})$, $M^{--}_{g0}(\vec{0})$ and $M^{--}_{gg}(\vec{0})$. Here only $R^{+,+}_{00}(\vec{g})$ needs a separate calculation performed at an "unusual" angle of incidence

given by $\vec{k}_{0//}+\vec{g}$. This must be repeated if another value $\vec{g}'$ is considered. Useful byproduct terms are $M^{+-}_{\vec{0}\vec{0}}(\vec{0})$, $M^{+-}_{\vec{0}\vec{g}}(\vec{0})$, $M^{+-}_{\vec{g}\vec{0}}(\vec{0})$ and $M^{+-}_{\vec{g}\vec{g}}(\vec{0})$.

4. The intensity of a beam $\vec{g}+\vec{G}$ ($\vec{g}$ and $\vec{G}$ both $\neq \vec{0}$) requires $R_{\vec{G}\vec{0}}(\vec{0})$, $R_{\vec{G}\vec{0}}(\vec{g})$, $M^{++}_{\vec{0}\vec{0}}(\vec{0})$, $M^{++}_{\vec{g}\vec{0}}(0)$, $M^{--}_{\vec{g}\vec{0}}(\vec{G})$ and $M^{--}_{\vec{g}\vec{g}}(\vec{G})$. Again, those elements with a non-zero vector $\vec{g}$ or $\vec{G}$ between the parentheses require a separate calculation for each desired value of $\vec{g}$ or $\vec{G}$. The useful byproducts are now $R_{\vec{0}\vec{0}}(\vec{0})$, $R_{\vec{G}\vec{0}}(\vec{0})$, $R_{\vec{G}\vec{G}}(\vec{0})$, $R_{\vec{0}\vec{0}}(\vec{g})$, $R_{\vec{0}\vec{G}}(\vec{g})$, $R_{\vec{G}\vec{G}}(\vec{g})$, $M^{+-}_{\vec{0}\vec{0}}(\vec{0})$, $M^{+-}_{\vec{g}\vec{0}}(\vec{0})$, $M^{+-}_{\vec{0}\vec{g}}(\vec{0})$, $M^{+-}_{\vec{g}\vec{g}}(\vec{0})$, $M^{+-}_{\vec{0}\vec{0}}(\vec{G})$, $M^{+-}_{\vec{g}\vec{0}}(\vec{G})$, $M^{+-}_{\vec{0}\vec{g}}(\vec{G})$ and $M^{+-}_{\vec{g}\vec{g}}(\vec{G})$.

The accuracy of the Beam Set Neglect method depends on the weakness of third-and higher-order multiple scattering (in the sense used in Fig. 2), which in turn depends on the weakness of back scattering by both the overlayer and the substrate, and on wave damping over the overlayer-substrate distance. The relatively complete calculations of Ref. 21 support the validity of this approach at least for Xe on Ag(111). For commensurate overlayers, where an "exact" calculation is possible, the method has been successfully tested with a variety of molecular overlayers on Rh(111) and Pt(111) substrates.[49-51] There are other ways to test the accuracy of Beam Set Neglect as applied to any given surface, without performing "exact" calculations. One way is to compare the intensities of the beams $\vec{0}$ and $\vec{G}$ calculated with just the set $\{\vec{G}\}$ and calculated with both sets $\{\vec{G}\}$ and $\vec{g}+\{\vec{G}\}$, for any $\vec{g}$; the $\vec{0}$ and $\vec{G}$ intensities should not change if the BSN assumptions are met exactly. Another related approach is to vary $\vec{g}$ and watch the change in the $\vec{0}$ and $\vec{G}$ intensities. Similarly, one may simultaneously use <u>three</u> rather than two

beam sets, e.g. $\{\vec{G}\}$, $\vec{g}+\{\vec{G}\}$ and $\vec{g}'+\{\vec{G}\}$, and watch the intensity of $\vec{g}$ and $\vec{g}+\vec{G}$ as $\vec{g}'$ is varied (or left out).

3.4 Structural Information Content

We next turn our attention to the structural information content of the different beam categories: $\vec{0}$, $\vec{G}$, $\vec{g}$ and $\vec{G}+\vec{g}$. This has already been discussed in the kinematic limit above, when we defined these categories. However, we must add, among others, the issue of registry, in the sense of the relative position of the overlayer with respect to the substrate parallel to the surface. Incommensurability makes the layer registry an undefined concept, since each overlayer atom has its own different and unique registry. Let us show that the registry indeed does not show up in the LEED theory. In the kinematic limit, only the specular beam is sensitive to the relative position of overlayer and substrate; moreover it is sensitive only to the layer spacing and not to the registry, because the momentum transfer is perpendicular to the surface (this is true even in the commensurate situation). In the presence of multiple scattering, we must determine whether any given exit beam can be reached by different pathways (thereby producing structure-sensitive interference) and what information these pathways carry. By inspecting the diagrams of Fig. 2, one finds that in each different multiple-scattering pathway leading to the same exit beam, the registry information is systematically cancelled out for incommensurate lattices. This is easily shown by example. If we choose an exit beam $\vec{G}$ (a substrate beam), it can be reached by scattering pathways such as the following, where we use the earlier defined layer diffraction matrices, a

right-to-left reading sequence, as in matrix multiplication, and plane-wave propagators $P^{\pm}_{\vec{G}}$ or $P^{\pm}_{\vec{g}}$, etc. between layers:

$M^{--}_{\vec{0}\vec{0}}(\vec{G})\ P^{-}_{\vec{G}}\ R_{\vec{G}\vec{0}}(\vec{0})\ P^{+}_{\vec{0}}\ M^{++}_{\vec{0}\vec{0}}(\vec{0})$, the 1st-order scattering term;

$M^{--}_{\vec{0}\vec{0}}(\vec{G})\ P^{-}_{\vec{G}}\ R_{\vec{G}\vec{G}'}(\vec{0})\ P^{+}_{\vec{G}'}\ M^{+-}_{\vec{0}\vec{0}}(\vec{G}')\ P^{-}_{\vec{G}'}\ R_{\vec{G}'\vec{0}}(\vec{0})\ P^{+}_{\vec{0}}\ M^{++}_{\vec{0}\vec{0}}(\vec{0})$, a 3rd-order scattering term;

$M^{--}_{\vec{0}\vec{g}}(\vec{G})\ P^{-}_{\vec{G}+\vec{g}}\ R_{\vec{G}\vec{0}}(\vec{g})\ P^{+}_{\vec{g}}\ M^{++}_{\vec{g}\vec{0}}(\vec{0})$, another 3rd-order scattering term.

The propagators $P^{\pm}$ are defined by reference to two points, one in the overlayer and one in the substrate, linked by a vector $\vec{r}$, which includes a registry $\vec{r}_{//}$: $P^{\pm}_{\vec{G}} = \exp(i\vec{k}^{\pm}_{\vec{G}}\cdot\vec{r})$ and similarly for $P^{\pm}_{\vec{g}}$ and $P^{\pm}_{\vec{G}+\vec{g}}$. A common feature of <u>all</u> the scattering terms of the type shown above (namely contributing to exit beam $\vec{G}$) is that the registry $\vec{r}_{//}$ survives only in a single multiplicative factor $\exp(-i\vec{G}\cdot\vec{r}_{//})$ originating in the leftmost $P^{-}_{\vec{G}}$ factor, because of otherwise canceling pairs of P^{+} and P^{-} factors. When the beam intensity is obtained by squaring the absolute value, this remaining factor $\exp(-i\vec{G}\cdot\vec{r}_{//})$ becomes 1 and the registry $\vec{r}_{//}$ has completely disappeared. The same argument applies to exit beams of type $\vec{g}$ or $\vec{G}+\vec{g}$.

While the registry cancels out as it should, there remains sensitivity to the interlayer spacing. As we shall now see, this sensitivity varies much between different beam types, unlike the commensurate case. The specular exit beam is always strongly sensitive to the interlayer spacing, as it is already in the kinematic limit. Multiple scattering adds to that sensitivity through weaker third- and higher-order terms.

A substrate beam $\vec{G}$, as Fig. 2 shows, receives its dominant contribution in direct scattering from the substrate. The overlayer only contributes through terms of third- or higher-order multiple scattering, which are relatively weak. Thus, to a good approximation, any $\vec{G}$ beam is primarily sensitive to the substrate structure: this allows the substrate structure to be determined without knowing the internal overlayer structure or the overlayer-substrate interlayer spacing. The close resemblance between the $\vec{G}$-beam I-V curves for a clean substrate and the same substrate covered with an incommensurate overlayer has been observed experimentally before for a Nb layer on Cu(100).[19] We have also confirmed it in the present work, with calculated I-V curves. A similar test is illustrated in Fig. 3 using Rh(111) as a substrate; the substrate-beam I-V curves are relatively insensitive to the position of the overlayer. Note that the degree of similarity of G-beam intensities for a clean and an overlayer covered surface is a measure of the weakness of higher-order multiple scattering terms. (However, relative peak heights can change, due to inelastic damping and Debye-Waller factors.)

An overlayer beam $\vec{g}$ is relatively more sensitive to the interlayer spacing through the interference of second- and higher-order terms with the first-order reflection from the overlayer (see Fig. 2).

A combination beam $\vec{G}+\vec{g}$, although intrinsically weak since it requires at least double scattering, is quite sensitive to the interlayer spacing through interference between the various second-order terms that contribute to it (see Fig. 2).

3.5 Calculational Scheme for Graphite Overlayers and Carbidic Overlayers

We shall consider the following model structures for graphite grown on Pt(111). First, we choose a single graphite layer over a bulk-terminated Pt(111) substrate. Here only the overlayer-substrate spacing needs to be determined. Second, we consider a single layer of carbon atoms occupying hollow sites of the Pt(111) substrate, in a commensurate (1x1) "carbidic" layer, overlain by a single graphite layer. Here the variables are the two interlayer spacings and the registry of the carbidic layer with respect to the substrate.

We shall only analyze the specular beam in this work. This should be sufficient since only one or two interlayer spacings are to be determined. Then only the beam set $\{\vec{G}\}$ is needed, and only the specular transmission and reflection amplitudes $M^{++}_{\vec{0}\vec{0}}(\vec{0})$ of the overlayer need to be computed, an easy task, even when multiple scattering is included within the overlayer. While only the specular substrate reflection $R^{++}_{\vec{0}\vec{0}}(\vec{0})$ is needed, the strong multiple scattering within the substrate requires, at least with Layer Doubling or Renormalized Forward Scattering, the calculation of all matrix elements $M^{\pm}_{\vec{G}',\vec{G}}(\vec{0})$ of the individual substrate layers. But this is a well-known conventional task.[47] Although the graphite overlayer is observed to adopt many orientations, this does not affect the specular beam intensity within the BSN approximation; we therefore use one arbitrary but fixed orientation in the calculation, namely overlayer and substrate lattices that are parallel to each other.

We use conventional non-structural parameter values in the calculations. For the Pt phase shifts, the relativistically-deduced (but spin-independent) phase shifts of Wang[52] were chosen, as discussed in Ref. 53. For the carbon atoms, both in graphitic and carbidic layers, we keep the phase shifts used in many hydrocarbon overlayer calculations, originally produced for acetylene bonded parallel to the Pt(111) surface.[54] Five phase shifts were used. A Debye temperature of 255 K was used for Pt, while the carbon atoms were given mean square vibration amplitudes double those of Pt.[53] Experimental data were collected and theoretical calculations were performed at 300 K. The damping was taken as an imaginary part of the energy, proportional to $E^{1/2}$, with a value of -3.8 eV at E = 90 eV. The muffin-tin zero was initially set at -14 eV, but later set free in the R-factor comparison with experiment. The R-factor analysis involved five R-factors and their average, as applied in many previous structure analyses.[55] The energy range common to theory and experiment was 20-235 eV, and data at three angles of incidence (θ=10°,15°,20° with ϕ=180°) were used.

4. Discrimination Against Incorrect R-factor Minima: Data Subdivision Method

The problem of multiple minima in R-factor comparisons between theory and experment is well known:[56,57] some incorrect structures can produce local minima in the R-factor and the issue is to find a method to discriminate against such inevitable occurrences. Of course, the deepest R-factor minimum should be the correct one, assuming that the correct

structure was included in the search. However, especially when approximations are applied, as we do here, there is no guarantee that the correct minimum has the lowest R-factor value.

A good example of multiple R-factor minima arises in this work. The metal-graphite interlayer spacing was initially allowed to vary over a considerable range of values: from 2.5 to 4.3 Å. Over this range several R-factor minima appear, as we illustrate in Section 6. We need to know which minimum corresponds to the actual interlayer spacing.

In Ref. 57, we have described several possible approaches to this problem, which we may collectively call data subdivision method. It compares and contrasts the structural results obtained with a series of individual subsets of the experimental data base. The subsets might be individual diffracted beams, or individual parts of the energy range, or data taken at individual angles of incidence. The underlying principle is this: the location of the correct R-factor minimum should not depend on the data set used. Therefore, any subset of the available data should yield the same structural result, except for statistical fluctuations due to the finite size of the data sets. By contrast, an incorrect R-factor minimum in general will shift markedly from one data subset to another. This is easily shown in our present application involving the determination of a layer spacing.

Assume for simplicity a kinematic theory applied to the specular beam at normal incidence for an overlayer at a height d_o above the substrate. If we take a small energy interval with an average wavelength of λ_1,

constructive interference between reflections by the overlayer and the substrate occurs when $2d_0 = n\lambda_1$ (n=0,1,2,...). This relation will, however, also be satisfied with a discrete set of different spacings $d = d_0 + \frac{1}{2}m\lambda_1$ (m=±1,±2,...). Thus, an R-factor will show minima not only at $d = d_0$, but also at $d = d_0 + \frac{1}{2}m\lambda_1$ (m=±1,±2,...). Let us now change the wavelength to λ_2, i.e. choose an energy interval with a different average wavelength. Then we again obtain an R-factor minimum at $d = d_0$, but now the other minima are at $d = d_0 + \frac{1}{2}m\lambda_2$ (m=±1,±2,...), which are shifted due to the change from λ_1 to λ_2. As a result, all the incorrect minima are identified by their shifts, while the correct one is stationary.

One may even utilize the fact that the shift $m(\lambda_2 - \lambda_1)/2$ of a minimum is proportional to its distance from the correct minimum. If one has not included the correct minimum in the structure search, by some oversight, it can in principle be simply obtained by extrapolation from the shifts of the incorrect minima.

This method of data subdivision will be shown in Section 6 to work extremely well in the case of graphite on Pt(111). It was already applied in the past as a test on the clean Rh(111) surface.[57] The case of data subdivision by individual beams has also been illustrated in Ref. 57, and was used extensively in many structural determinations since.[55]

5. Experiments for Graphite on Platinum

Incommensurate, ring-like electron diffraction patterns, attributed to graphitic carbon overlayers, have been observed on the (111), (110),[58] and (100)[59] surfaces of platinum single crystals. The observed ring radii match the lattice constant for the (0001) basal plane of bulk graphite,[60] and the Auger lineshape indicates that graphitic carbon is present on the surface.[43] The characteristic rings seen in the LEED pattern correspond to incommensurate sheets of graphite in randomly oriented domains. Several different preferred orientations of the graphite overlayer domains have been observed on the different faces of platinum.[25]

A graphitic carbon layer can be produced on a platinum crystal surface under ultra-high vacuum conditions either by exposing a hot platinum crystal to carbon-containing molecules, or by adsorbing carbon-containing molecules on a crystal at or below room temperature, and then annealing the crystal. Graphite layers have been produced on the Pt(111) surface from the decomposition of ethylene, cyclohexane, n-heptane, benzene, toluene,[23] propylene and butene. Heating a Pt(111) surface after hydrocarbon chemisorption results in selective dehydrogenation of the adsorbed molecules between 400 and 800 K. After annealing at a temperature sufficient for complete dehydrogenation of the chemisorbed molecules, the LEED pattern shows characteristic graphite rings. If the Pt(111) surface is heated above ~1150 K the surface carbon starts to dissolve into the bulk platinum; after sustained heating above 1150 K the graphite diffraction pattern is no longer visible, and Auger measurements show only a small amount of residual carbon on the surface.

Certain preferred orientations exist for graphite domains on Pt(111).[25] Typical diffraction patterns are shown in Fig. 4. The rings in the graphite diffraction pattern have a well-defined radius; the radial width of the rings is approximately the same as the width of the substrate diffraction spots, indicating long range crystalline order on the scale of the instrument response function (~100 Å). When a hydrocarbon covered crystal is annealed at successively higher temperatures, the diffraction rings first appear with relatively isotropic intensity. As the annealing temperature increases, the rings break up into bright segments, often with a dim continuous ring joining the segments, indicating some orientations are preferred. We have observed at least four different preferred orientations of the carbon rings on Pt(111). Usually the length of a bright arc on the carbon diffraction rings is several times its radial width. Approximate coincidence between the graphite and the platinum lattices has been suggested as the reason for the preferential orientation of graphite domains on Pt(111).[25]

Graphite layers can apparently grow by island formation on Pt(111). A clean Pt(111) surface at 1100 K was initially exposed to a small amount (1 Langmuir) of propylene (C_3H_5) vapor at 5×10^{-8} torr. When the crystal was cooled, segmented graphite rings were already visible in the LEED pattern with the same sharpness as the substrate diffraction spots.

As the crystal was exposed to increasing amounts of propylene vapor under the same conditions in increments of one Langmuir, the only change in the diffraction pattern was an increase in the brightness of the graphite diffraction features. The ratio of the carbon 272 eV peak to the platinum 237 eV peak (measured with a retarding field energy analyzer in the second-derivative mode at 10 V peak-to-peak modulation) increased approximately linearly with propylene exposure.

After a total exposure of 11 Langmuirs of propylene, weak diffraction features due to multiple scattering between the platinum substrate and the graphite overlayer became visible (see Fig. 4a). The C/Pt Auger peak height ratio was 3.4. The multiple-scattering features of the pattern were at least an order of magnitude weaker than the single scattering features due to the overlayer. Exposure to 13 Langmuirs of propylene increased the C/Pt Auger ratio to ~3.7; no further change in the C/Pt ratio or the LEED pattern occurred with increased hydrocarbon exposure. This apparent saturation of the graphite coverage in ultra-high vacuum conditions is consistent with results obtained from carbon monoxide decomposition.[61] We associate this coverage (C/Pt ratio of ~3.7) with a single complete graphite sheet on the Pt(111) surface.

We have observed graphite rings on a Pt(111) crystal with a C/Pt ratio significantly larger than 3.7 after the crystal was exposed to atmosphere, then mounted in the vacuum system and baked out. During bakeout the crystal was exposed to background gases at ~10^{-6} Torr and 500 K for several days. Diffraction spots from the platinum substrate

were almost invisible, and the graphite rings were continuous, with no sign of the angular variation in intensity typical of graphite produced under ultra-high vacuum conditions.

Our graphite/platinum experiments were conducted in a standard, bakeable, ion-pumped, stainless steel ultra-high vacuum system. This system was equiped with a four-grid LEED optics, which was also used for Auger measurements, and a quadrupole mass spectrometer. The Pt(111) single crystal was spot-welded to tantalum foil strips and mounted on a manipulator capable of independent azimuthal and co-latitude rotations. The crystal could be heated to 1500 K by passing a current through the supports, and cooled to 130 K by conduction from a pair of liquid nitrogen reservoirs. The crystal temperature was monitored using a 0.005" chromel-alumel thermocouple spot-welded to the edge of the crystal.

Sulfur was the main trace impurity at the crystal surface, along with very small amounts of calcium and silicon. Surface carbon was also present from gas phase contamination of the surface. The platinum crystal was cleaned by 500 eV argon ion sputtering at a crystal temperature of 1000 K and an argon pressure of 5×10^{-5} torr, followed by reaction with 2×10^{-7} torr of oxygen at a crystal temperature of 1000 K. After cleaning, the crystal was annealed at 1300 K. With this procedure we reproducibly obtained a surface where the concentration of all impurities was below the Auger detection threshold, and where a sharp, well-ordered LEED pattern with a low background could be observed.

The crystal was first oriented within 0.3 degrees of normal incidence, as determined by observation of the intensities of symmetrically degenerate diffraction beams. The angle of incidence was set by rotating the crystal away from the normal incidence position according to a scale inscribed on the crystal manipulator. The azimuthal angle was set at 180° (using the convention of Adams et al.[62]) in order to preserve a mirror plane symmetry in the diffraction pattern. The accuracy of the azimuthal angle setting could be verified through comparison of the measured intensities of symmetrically degenerate diffraction beams.

LEED patterns were measured for both the clean and graphite covered platinum surfaces at 10°, 15°, and 20° angles of incidence and an azimuthal angle of 180°. All LEED data were recorded at a crystal temperature of 300 K by LEED optics enclosed within a set of Helmholtz coils.

The LEED data for the graphite-covered surface were taken after exposing the Pt(111) crystal at 300 K to benzene vapor for 60 seconds at 5×10^{-7} torr (uncorrected ion gauge reading). This nominal 30 Langmuir benzene exposure saturates the Pt(111) surface at 300 K. The crystal was then annealed at 1100 K for 120 seconds, producing the characteristic graphite ring diffraction pattern. To increase the intensity of the graphite diffraction features the partly graphite-covered platinum crystal was exposed to an additional 30 Langmuirs of benzene vapor at

300 K, and then annealed a second time at 1100 K for 120 seconds. This procedure resulted in a diffraction pattern with bright, easily visible diffraction rings. The carbon (272 eV) to platinum (237 eV) Auger peak-height ratio was 1.44.

The LEED pattern data were collected using a high-sensitivity vidicon camera, and recorded on video tape. This video tape was then analyzed using a real-time, computer-interfaced, video image digitizer system and analysis software developed in our laboratory.[63]

I-V data were recorded from 10 to 400 eV at each angle of incidence. The theoretical analysis of the data is based on the I-V curve of the specularly reflected beam. I-V curves for at least three additional non-degenerate substrate diffraction beams were compared at each angle of incidence, in order to allow investigation of the effects of the graphite overlayer on the structure of the platinum substrate (see Section 6). I-V curves from a pair of degenerate beams were compared at each angle of incidence in order to verify the mirror plane symmetry corresponding to a 180° azimuthal angle of incidence.

6. Structural Analysis

To analyze the structure of graphite on Pt(111), we first examined the experimental substrate beams. These should exhibit the substrate structure, with little influence by the overlayer on the diffraction. Fig. 5 compares the measured substrate-beam I-V curves for

graphite-covered and clean Pt(111). Their close similarity indicates that the substrate has not markedly changed its structure upon graphite addition. The similarity of I-V curves also implies that third-order scattering is relatively weak in this system. Otherwise, large differences would occur. Some minor differences are apparent in Fig. 5: these are partly due to multiple scattering effects, and partly to the additional damping of the overlayer; a much larger source of differences could be the presence of intercalated carbon in a (1x1) lattice on the metal surface, evidence for which we shall present below. Experimental variations in the angle of incidence between the clean and graphite overlayer data sets is another possible source of differences.

Based on these various observations, we assume a bulk-like Pt(111) surface (since the clean Pt(111) surface is unrelaxed within the LEED accuracy[53]), and an incommensurate graphite overlayer, with possibly an intercalated chemisorbed carbon layer. Other models seem far less likely: additional graphite layers would rapidly obliterate the substrate beams; a high density of carbon atoms within the metal surface would change the substrate structure. Various carbonaceous fragments are most likely present, but only in a disordered manner, not contributing significantly to the measured intensities.

The first model, a graphite monolayer without intercalated carbon, gives rise to the R-factor plots of Fig. 6 as the graphite-metal distance is varied. Multiple R-factor minima are clearly visible. We have varied

the energy range used in the R-factor calculation, yielding different average wavelengths, to uniquely identify the correct minimum, as described in Section 4; Fig. 6 shows that the correct minimum occurs at d_{Pt-gr} = 3.70±0.05 Å. The best value of the five-R-factor average was 0.150.

The other model, with intercalated carbon chemisorbed either in fcc-type hollow sites or in hcp-type hollow sites of Pt(111), was tested in the same manner. The metal-carbon d_{Pt-C} spacing was varied through the range 1.2 to 1.6 Å, since its value is near 1.30 Å for ethylidyne in hollow sites on Pt(111)[64] and Rh(111),[65,66] and near 1.45 Å for CO in hollow sites on Rh(111);[51,67] this is also consistent with metal-carbide bond lengths. The carbon-graphite spacing d_{C-gr} was varied through the range 2.0 to 3.0 Å. In both cases (fcc and hcp-sites for carbon), the optimum layer spacings were d_{Pt-C} = 1.25±0.10 Å and d_{C-gr} = 2.45±0.10 Å, with a smaller uncertainty on their sum $d_{Pt-gr} = d_{Pt-C} + d_{C-gr}$ = 3.70±0.05 Å (the two partial spacings are rather strongly correlated in the LEED analysis, in such a way that their sum is more reliable than each one taken separately). A contour plot for the five-R-factor average is shown in Fig. 7 for the hcp hollow site. The best five-R-factor value is 0.154 for both of these models, hardly different from the graphite-only case. Note that the best metal-graphite distance is the same in all three models. The best-fit value for the muffin-tin zero was -16±1 eV. Fig. 8 shows comparisons of I-V curves for near-optimal structures for each model.

7. Discussion and Conclusions

7.1 Theoretical Methods

We have shown the applicability of the Beam Set Neglect approach to LEED calculations for incommensurate overlayers. It relies on the neglect of certain third- and higher-order scattering events. Their weakness is thus verified in the case of graphite on Pt(111), even though this is a priori a relatively unfavorable system: platinum is a strong scatterer due to its large atomic number,[2] as is the graphitic layer due to its high atomic density.

The main advantage of the Beam Set Neglect method is the reduction of computational effort that it brings. Also it fits very easily within conventional LEED theory, being very similar to the treatment of (2x1) or c(2x2) overlayers, in the sense of needing two beam sets rather than the single integral-order beam set.

We wish to emphasize the attractive feature, particular to incommensurate systems, that the substrate beam intensities are largely insensitive to the overlayer position and geometry. This allows the substrate geometry to be determined first, before tackling the overlayer structure. Such a separation of the structural problem is unusual in LEED, where normally all structural parameters must be determined simultaneously.

The data subdivision method has been most useful in resolving the correct structure in the presence of several R-factor minima. It has been applied here to a relatively small data set, consisting of just the

specular beam, by subdividing the available energy range to obtain different average wavelengths. Other subdivisions, by beams or by incident angles, have already been extensively used in the past.

It should be noted that we attempted the CMTA-Fourier transform approach,[12] mentioned in Section 2. It did not succeed, probably because that approach requires weaker multiple scattering than is present in graphite/Pt(111), and because we averaged over only 3 spectra in the CMTA step and thus had little chance of sufficiently reducing multiple scattering contributions.

7.2 Structural Results

We have postulated three likely models for the structure of graphite on Pt(111) and they all agree equally well with experiment. There is a common feature between the three models: the best graphite-metal distance is 3.70 Å in each. There is also a common feature between the two models involving intercalated carbon: the layers spacings remain equal as the carbon atoms are moved from one type of hollow site to the other. As we shall see below, a graphite-metal spacing of 3.70 Å is implausibly large, unless the graphite is supported at that height by some intercalates. So we propose that the actual structure is composed of the three models in unknown proportions (see Fig. 9). Namely, there are carbon atoms in hollow sites of Pt(111) at a height of 1.25 Å. They possibly, but not necessarily, occur in both types of hollow sites. They may be distributed in domains of well-ordered (1x1) structure covering a part of the surface, or they may be randomly distributed among hollow sites (lattice-gas disorder). Supported by this intercalated carbon

layer is the graphite layer at a height of 2.45 Å above the carbon plane. We do not claim that this structure gives a complete description of the actual situation, but is its major component. Some carbon atoms may have interstitially penetrated the metal lattice (without appreciably changing its geometry, as we have discussed), others may lie on the Pt surface without being covered by graphite. The graphite itself seems to exist mainly in the form of rotationally disordered sheets large enough to produce sharp diffraction rings, i.e. with linear dimensions of at least ~100 Å. However, we do not rule out the possibility of various smaller graphite fragments tilted in many possible ways with respect to the surface plane, as well as of other disordered carbonaceous fragments.

Our numerical results for layer spacings may be compared with other situations where bond distances or bond lengths are known. First, the intercalated carbon has a metal-carbon bond length of 2.03±0.07 Å. This may be compared with a value of 2.00±0.07 Å obtained for the terminal carbon of ethylidyne (CCH_3) which is also bonded in a hollow site of Pt(111).[64] Similar values are obtained for ethylidyne on Rh(111), with[66] and without[65] coadsorbed CO and for CO adsorbed in a hollow site, e.g. for CO coadsorbed with benzene[51] or with ethylidyne[66] on Rh(111), where the metal-carbon bond length appears to be more variable, from 2.03±0.07 Å to 2.12±0.07 Å (the corresponding metal-carbon layer spacings are 1.30±0.1 Å for ethylidyne in hollow sites compared with 1.30±0.10 Å to 1.45±0.10 Å for CO in hollow sites). Based on bond lengths, we propose that the intercalated carbon is strongly bonded to the metal, similar to ethylidyne.

7.3 The Nature of the Graphite-Substrate Interaction

We address here the issue whether the graphite layer is physisorbed, chemisorbed or bonded with intermediate strength to the substrate.

The metal-graphite and carbon-graphite spacings can give us a clue to the nature of the bonding in this system. First, we may compare our result for the spacing d(Pt-graphite) of 3.70±0.10 Å with that obtained by SEELFS[39] for commensurate graphite on Ni(111), namely a spacing d(Ni-graphite) of 2.80±0.08 Å. This already points to an abnormally large Pt-graphite spacing. Other evidence comes from layer spacings for rare gas monolayers on metal surfaces, namely Xe on Ag(111)[12,14] with d(Ag-Xe) = 3.55±0.1 Å. Replacing the radius of Ag by Pt and Xe by graphite, and using covalent metallic radii for the metals and Van der Waals radii for both xenon (2.18 Å) and graphite (1.67 Å) we predict d(Pt-graphite) ~ 2.96 Å. Other known spacings, such as those for Ar and Kr on graphite,[4] with d(Ar-graphite) = 3.20±0.10 Å and d(Kr-graphite) = 3.30±0.10 Å, also lead to similar predictions for graphite on Pt(111). By contrast, if we accept intercalated carbon with d(Pt-C) = 1.25 Å and a covalent carbon radius of 0.77 Å for single bonds, a much better result emerges. Then we predict for the platinum-graphite spacing d(Pt-C-graphite) = 1.25 + 0.77 + 1.67 = 3.69 Å, which agrees well with our result of 3.70±0.10 Å. No comparable agreement can be obtained with the Van der Waals radius for the chemisorbed carbon (1.75 Å).

In an attempt to explain the various layer spacings mentioned above in a consistent and simple fashion, we have found that the following rules predict the observed interlayer spacings. In general we expect these predictions to be accurate within ~ 0.2 Å.

1. When two inert layers (which favor Van der Waals bonding) are joined, Van der Waals radii of course explain the observed layer spacings well. Thus, d(Ar-graphite) = ½d(Ar-Ar) + ½d(graphite-graphite) = 1.56 + 1.67 = 3.23 Å vs the observed 3.30±0.10 Å; for d(Ar-Ar) we use here the (111) interlayer spacing of bulk fcc Ar.

2. When one layer of inert character is joined to a layer which is not inert, as in graphite on a metal surface, one should use Van der Waals radii for the inert layer and a covalent (or ionic) radius for the other layer; the latter covalent or ionic radius is taken to represent an average over the surface corrugation for close-packed surfaces. Thus d(Ag-Xe) = 1.32 + 2.18 = 3.50 Å vs the observed 3.50±0.010 Å; here the Ag radius of 1.32 is the average of the metallic radius of 1.44 Å and half the (111) interlayer spacing of bulk fcc Ag, which is 1.18 Å. The corresponding values for graphite on carbon-covered platinum have been given above, using the carbon covalent radius.

Thus, a combination of Van der Waals and covalent radii are needed to explain the observed layer spacings for graphite on Pt(111). We would, therefore conclude that the graphite layer is bonded to the substrate

with a strength intermediate between physisorption and chemisorption. One may wonder whether such bonding might lead to rehybridization of the graphitic carbon atoms and a distortion of the graphite layer, including a change in its lattice constant. However, it is known that no such effect takes place in bulk[67] and surface[68] graphite intercalate structures, even though substantial charge transfer is known to occur there between the intercalate (e.g. alkali atoms) and the graphite layers.

Acknowledgments

We thank C. T. Kao and G. S. Blackman for many fruitful discussions.

This work was supported by the Director, Office of Energy Research, Office of Basic Energy Sciences, Materials Sciences Division of the U.S. Department of Energy under Contract No. DE-AC03-76SF00098.

References

1. Strict mathematical irrationality of a lattice constant ratio cannot be proved experimentally, due to finite sample sizes (mosaic structure) and finite instrumental response widths. Also, strict irrationality probably does not exist between layers that are bound together. The reason is that their non-vanishing mutual interaction should impose commensurability with a sufficiently large coincidence unit cell, either through a lattice constant change or through dislocations or domain boundaries. Nevertheless, we shall use the term "incommensurate lattices": we shall define it to apply to any overlayer that does not show a coincidence lattice with the substrate within the sample size or the instrumental response width.
2. "Ordering in Two Dimensions", Ed. S.K. Sinha, Elsevier North Holland (New York) 1980.
3. G.L. Price and J.A. Venables, Phys. Letters 47A, 9 (1974).
4. C.G. Shaw, S.C. Fain, Jr., M.D. Chinn and M.F. Toney, Surf. Sci. 97, 128 (1980).
5. M.D. Chinn and S.C. Fain, Jr., Phys. Rev. Letters 39, 146 (1977); S.C. Fain, Jr., M.D. Chinn and R.D. Diehl, Phys. Rev. B21, 4170 (1980).
6. R.D. Diehl and S.C. Fain, Jr., Surf. Sci. 125, 116 (1983).
7. J. Perdereau and G.E. Rhead, Surf. Sci. 24, 555 (1971).
8. P.W. Palmberg, Surf. Sci. 25, 104 (1971).
9. M.A. Chesters, M. Hussain and J. Pritchard, Surf. Sci. 35, 161 (1973); Surf. Sci. 54, 687 (1976).
10. A. Ignatiev, T.N. Rhodin and S.Y. Tong, Surf. Sci. 42, 37 (1974).

11. M.F. Bridge, R.A. Marbrow and R.M. Lambert, Surf. Sci. 57, 415 (1976).

12. P.I. Cohen, J. Unguris and M.B. Webb, Surf. Sci. 58, 429 (1976).

13 L.W. Bruch, P.I. Cohen, and M.B. Webb, Surf. Sci. 59, 1 (1976).

14. N. Stoner, M.A. Van Hove, S.Y. Tong and M.B. Webb, Phys. Rev. Letters 40, 243 (1978).

15. J. Unguris, L.W. Bruch, E.R. Moog and M.B. Webb, Surf. Sci. 109, 522 (1981).

16. L.L. Atanososka, J.C. Buchholz and G.A. Somorjai, Surf. Sci. 72, 189 (1978).

17. Z.P. Hu and A. Ignatiev, Phys. Rev. B30, 4856 (1984).

18. Z.P. Hu, N.J. Wu and A. Ignatiev, to be published.

19. W.S. Yang and F. Jona, Surf. Sci. 109, L505 (1981).

20. E.L. Garfunkel and G.A. Somorjai, Surf. Sci. 115, 441 (1982).

21. M.A. Van Hove, R.J. Koestner, P.C. Stair, J.P. Bibérian, L.L. Kesmodel, I. Bartoš and G.A. Somorjai, Surf. Sci. 103, 189 (1981).

22. J.G. McCarty and R.J. Madix, J. Catal. 38, 402 (1975).

23. K. Baron, D.W. Blakeley and G.A. Somorjai, Surf. Sci. 41, 45 (1974).

24. J.L. Gland and G.A. Somorjai, Surf. Sci. 41, 387 (1974).

25. B. Lang, Surf. Sci. 53, 317 (1975).

26. D.G. Castner, B.A. Sexton and G.A. Somorjai, Surf. Sci. 71, 519 (1978).

27. C. Leygraf and S. Ekelund, Surf. Sci. 40, 609 (1973).

28. P.H. Holloway and J.B. Hudson, Surf. Sci. 43, 141 (1974).

29. P. Légaré, G. Maire, B. Carriere and J.P. Deville, Surf. Sci. 68, 348 (1977).

30. R. Bastasz, C.A. Colmenares, R.L. Smith, and G.A. Somorjai, Surf. Sci. 67, 45 (1977).

31. W.N. Unertl and J.M. Blakely, Surf. Sci. 69, 23 (1973).

32. S. Ekelund and C. Leygraf, Surf. Sci. 40, 179 (1973).

33. A. Glachant, J.P. Coulomb and J.P. Bibérian, Surf. Sci. 59, 619 (1976).

34. F.P. Netzer and M. Prutton, Surf. Sci. 52, 505 (1972).

35. N.R. Avery, Surf. Sci. 41, 533 (1974).

36. P.A. Lee, P.H. Citrin, P. Eisenberger and B.M. Kincaid, Rev. Mod. Phys. 53, 769 (1981).

37. J.J. Barton, C.C. Bahr, Z. Hussain, S.W. Robey, J.G. Tobin, L.E. Klebanoff, and D.A. Shirley, Phys. Rev. Lett. 51, 272 (1983).

38. T.L. Einstein, Appl. Surf. Sci. 11/12, 42 (1982).

39. R. Rosei, M. de Crescenzi, F. Sette, C. Quaresima, A. Savoia and P. Perfetti, Phys. Rev. B28, 1161 (1983).

40. L. Papagno and L.S. Caputi, Phys. Rev. B29, 1483 (1984).

41. G.A. Somorjai, "Chemistry in Two Dimensions: Surfaces", Cornell Univ. Press, Ithaca (1981).

42. M.A. Van Hove and S.Y. Tong, Surf. Sci. 52, 673 (1975); J.F. Onuferko, D.P. Woodruff and B.W. Holland, Surf. Sci. 87, 357 (1979); K.H. Rieder and H. Wilsch, Surf. Sci. 131, 245 (1983); T.S.Rahman and H. Ibach, Phys. Rev. Letters 54, 1933 (1985).

43. T.W. Haas, J.T. Grant, and G.T. Dooley III, J. Appl. Phys. 43, 1853 (1972).

44. M.P. Hooker and G.T. Grant, Surf. Sci. 62, 21 (1977).

45. S.M. Davis and G.A. Somorjai, J. Catal. 65, 78 (1980).

46. We exclude the case where the incommensurability occurs only in one surface dimension, while the other surface dimension presents a

commensurate relationship. An example is generated by starting with a (1x1) overlayer and compressing it uniaxially only. This situation is easily treated as a special case of the general incommensurability that we are concerned with in this paper.

47. M.A. Van Hove and S.Y. Tong, "Surface Crystallography by LEED", Springer (Heidelberg), 1979.
48. M.A. Van Hove and G.A. Somorjai, Surf. Sci. 114, 171 (1982).
49. M.A. Van Hove, R.F. Lin and G.A. Somorjai, Phys. Rev. Letters, 51, 778 (1983).
50 M.A. Van Hove, R.J. Koestner, J.C. Frost and G.A. Somorjai, Surf. Sci. 129, 482 (1983).
51. M.A. Van Hove, R.F. Lin and G.A. Somorjai, to be published.
52. S.W. Wang, private communication.
53. D.F. Ogletree, M.A. Van Hove and G.A. Somorjai, Surf. Sci. in press.
54. L.L. Kesmodel, R.C. Baetzold, and G.A. Somorjai, Surf. Sci. 66, 299 (1977).
55. R.J. Koestner, M.A. Van Hove and G.A. Somorjai, Surf. Sci. 107, 439 (1981).
56. S. Andersson and J.B. Pendry, Sol. St. Commun. 16, 563 (1975).
57. M.A. Van Hove and R.J. Koestner, in "Determination of Surface Structure by LEED", Eds. P.M. Marcus and F. Jona, Plenum Press (New York) 1984, p.357.
58. H.B. Lyon and G.A. Somorjai, J. Chem. Phys. 46, 2539 (1967).
59. A.E. Morgan and G.A. Somorjai, Surf. Sci. 12, 405 (1968).
60. J.W. May, Surf. Sci. 17, 267 (1969).
61. J.P. Biberian and G.A. Somorjai, Appl. of Surf. Sci. 2, 352 (1979).

62. D.L. Adams, H.B. Nielsen, and M.A. Van Hove, Phys. Rev. B20, 4789, (1970).

63. D.F. Ogletree, J.E. Katz, G.A. Somorjai, to be published.

64. L.L. Kesmodel, L.H. Dubois and G.A. Somorjai, J. Chem. Phys. 70, 2130 (1979).

65. R.J. Koestner, M.A. Van Hove and G.A. Somorjai, Surf. Sci. 121, 321 (1982).

66. R.J. Koestner, M.A. Van Hove and G.A. Somorjai, to be published.

67. M.S. Dresselhaus and G. Dresselhaus, Adv. Phys. 30, 139 (1981).

68. N.J. Wu and A. Ignatiev, Phys. Rev. B28, 7288 (1983).

Figures

Fig. 1 a. Basic beam types in the presence of an incommensurate overlayer on a substrate.

b. Corresponding reciprocal lattice vectors in the surface plane, including a combination vector (beam) $\vec{G}+\vec{g}$ (only one overlayer domain is shown).

Fig. 2 Classification of multiple-scattering paths for an incommensurate overlayer with reciprocal lattice $\{\vec{g}\}$ on a substrate with reciprocal lattice $\{\vec{G}\}$. Rows indicate type of exit beam: $\vec{0},\vec{G},\vec{g}$ or $\vec{g}+\vec{G}$. Columns indicate order of multiple scattering as defined in text. (All multiple scattering is included exactly within the overlayer taken by itself and also within the substrate taken by itself; forward scattering is not counted as multiple scattering here.) Beam Set Neglect includes the first two columns.

Fig. 3 Theoretical I-V curves for the substrate beams $\vec{G}$ = (10) and (01) for incommensurate graphite on Rh(111) at normal incidence. The graphite-metal layer spacing is varied from 3.05 to 3.85 Å. Intensities are normalized to the same maximum peak height for each curve, with vertical offsets for clarity. (No intercalated carbon (1x1) layer is included in this calculation).

Fig. 4 LEED patterns of graphitic carbon on Pt(111). Graphite domains exhibit a number of different orientations with the platinum substrate. The observed orientation has no obvious relation to the conditions under which the graphite was formed.

(a) The bright ring segments indicate two preferred domain orientations of graphite on Pt(111). This is the graphite orientation observed most often on Pt(111). Weak streaks near the bright center (specular) beam are due to $\vec{G}+\vec{g}$ combination beams. These beams show the weakness of second- and higher-order scattering. The Pt crystal was exposed to 12 Langmuir of propylene at 1100 K (C/Pt Auger ratio 3.3).

(b) Several graphite ring-features are shown. Three domain orientations dominate this image. The Pt crystal was exposed to 9 L of propylene at 1100 K (C/Pt Auger ratio 3.5).

(c) Two different domain orientations on Pt(111). The Pt crystal was saturated with proplyene at room temperature, then annealed to 1150 K.

(d) Several graphite domain orientations on Pt(111). $\vec{G}+\vec{g}$ multiple scattering features are visible near the substrate beams. The Pt crystal was exposed to 25 L of benzene at room temperature, annealed at 1100 K, exposed to an additional 25 L of benzene at room temperature, then annealed at 1100 K for 180 seconds (C/Pt Auger ratio 1.45). This picture was taken after recording LEED I-V data for the graphite-covered platinum (111) surface.

Fig. 5 Experimental I-V spectra of substrate beams for clean (thin lines) and graphite-covered (thick lines) Pt(111) at two polar angles at incidence (as marked) and at azimuth $\phi = 180^{\circ}$. Within each of the six graphs the intensities are drawn to the same scale, which, however, varies arbitrarily from graph to graph.

Fig. 6 Five-R-factor average for a graphite monolayer on Pt(111) as a function of graphite-metal layer spacing. Different energy ranges, as shown, are used to generate the different curves; corresponding average wavelengths are shown. The three upper curves have been shifted upwards for clarity. In this and similar data at other angles of incidence, the minima at $d \sim 3.7^{\circ}$ Å line up most consistently.

Fig. 7 Contour plot of the five-R-factor average for the specular beam at $(\theta,\phi) = (15^{\circ},180^{\circ})$ diffracted by an incommensurate graphite monolayer on a (1x1) carbon layer chemisorbed in hcp hollow-sites on Pt(111). The muffin-tin zero is at -16 eV below vacuum. The cross marks the approximate location of the minimum R-factor.

Fig. 8 Experimental (dashed) and near-optimal theoretical (full) I-V curves for the specular beam for incommensurate graphite on Pt(111) with and without an intercalated commensurate (1x1) carbon layer. The chemisorbed carbon atoms occupy either hcp- or fcc-hollow sites of the Pt(111) substrate. The theoretical

curves show different combinations of layer spacings and the corresponding five-R-factor-average values. Intensities are normalized to the same maximum peak height for each curve, with vertical offsets for clarity.

Fig. 9 Model of an incommensurate graphite monolayer on Pt(111), including intercalated (1x1) carbon islands in two types of hollow sites. Optimum layer spacings are shown.

Incommensurate beams and patterns

a) Beam types

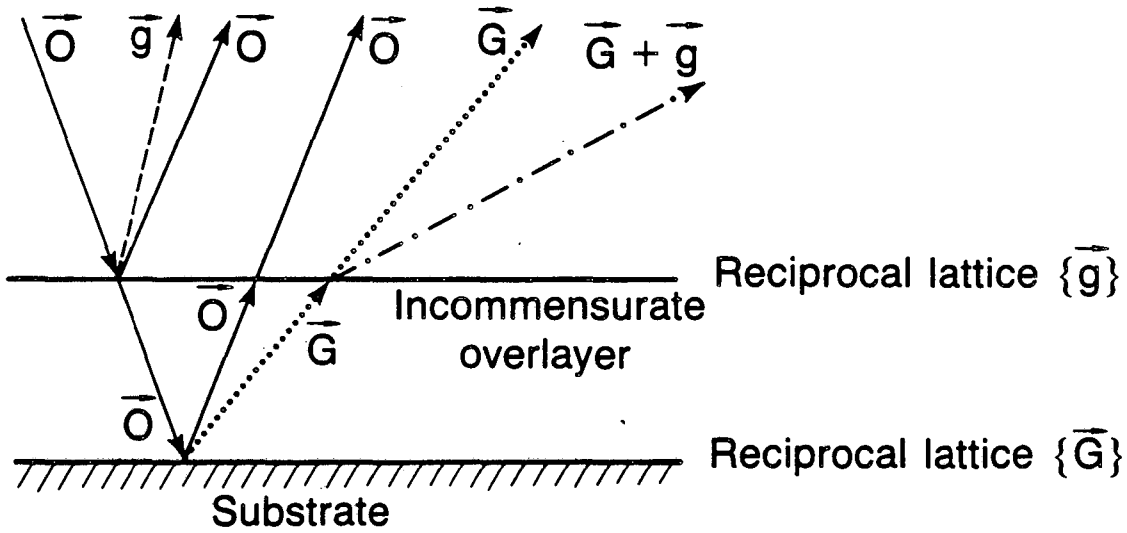

b) Reciprocal lattices

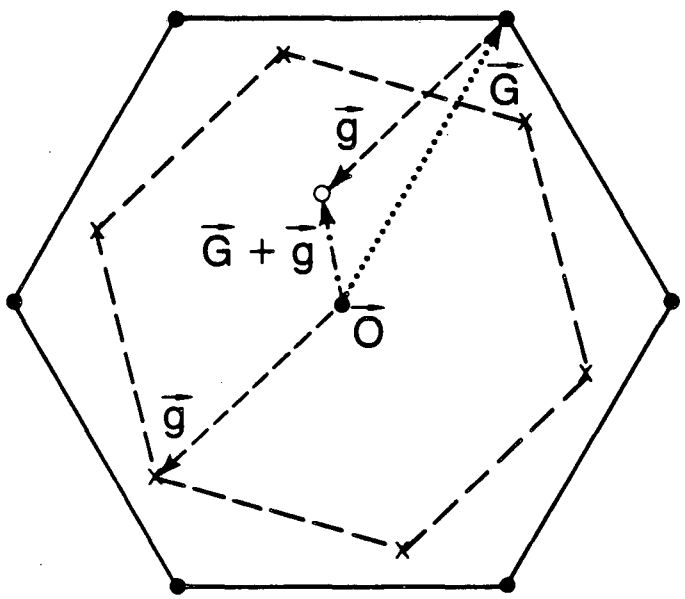

XBL 8512-12790

Fig. 1

Incommensurate overlayers: beam type vs. order of scattering

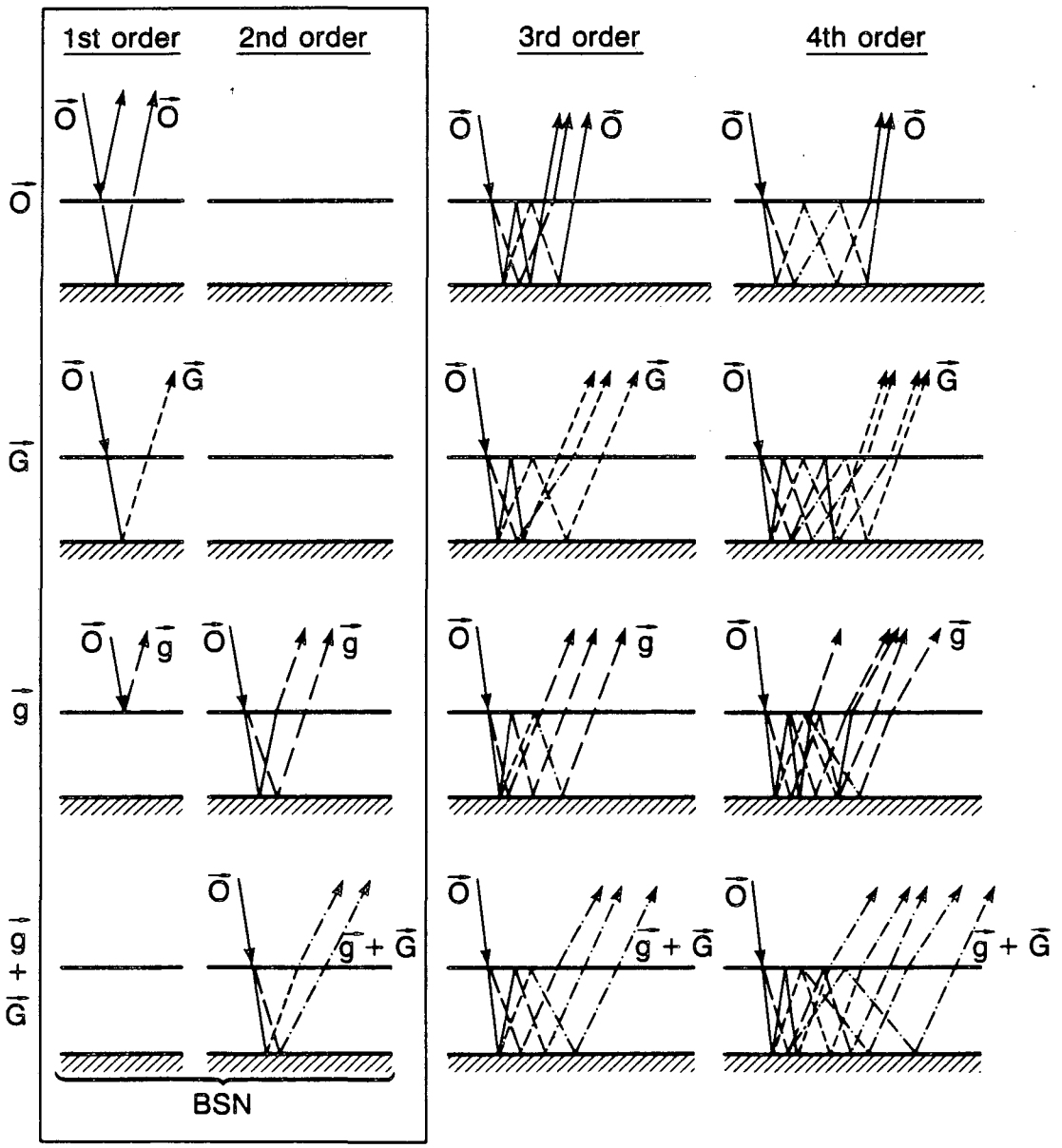

XBL 8512-12792

Fig. 2

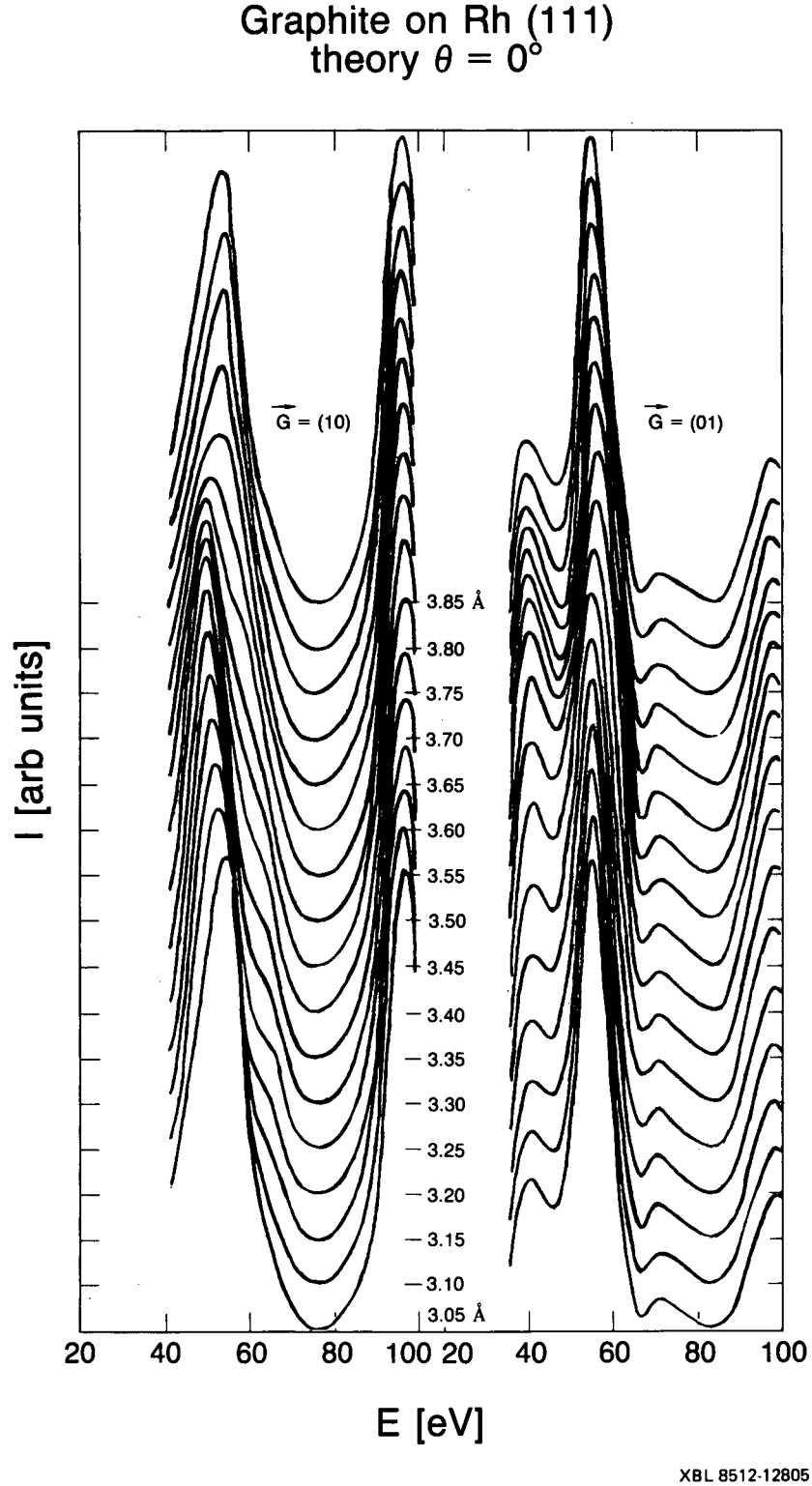
Graphite on Rh (111)
theory θ = 0°
G = (10)
G = (01)
3.85 Å
3.80
3.75
3.70
3.65
3.60
3.55
3.50
3.45
3.40
3.35
3.30
3.25
3.20
3.15
3.10
3.05 Å
I [arb units]
20
40
60
80
100
20
40
60
80
100
E [eV]
XBL 8512-12805

Fig. 3

LEED Patterns of Graphite on Pt(111)

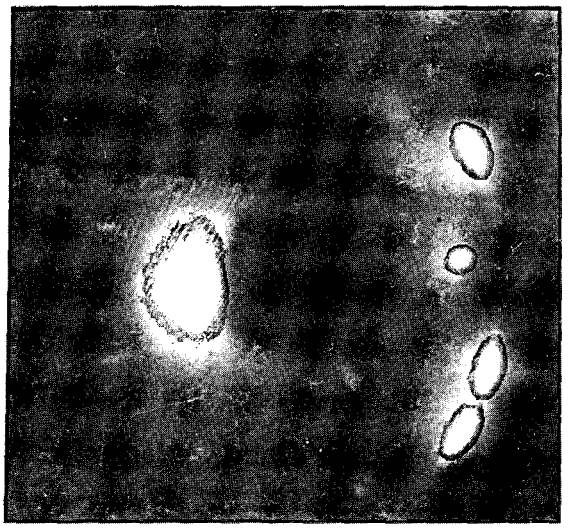

a) 46 eV at −10°

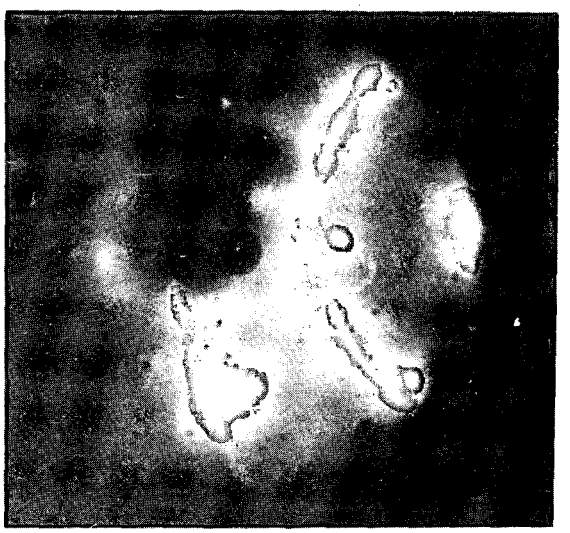

b) 64 eV at 35°

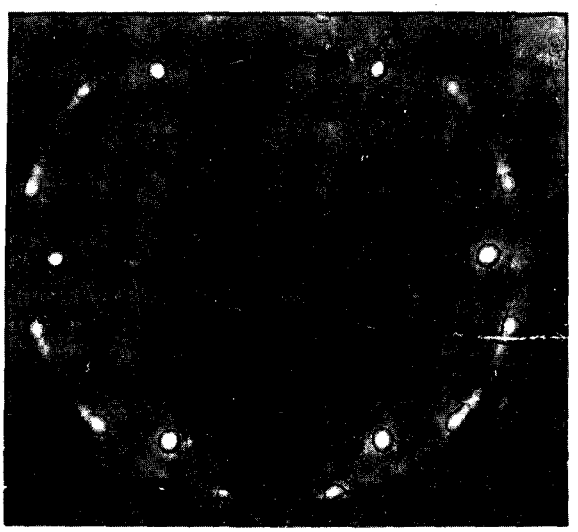

c) 55 eV at 0°

d) 45 eV at 11°

Fig. 4

XBB 864-3003

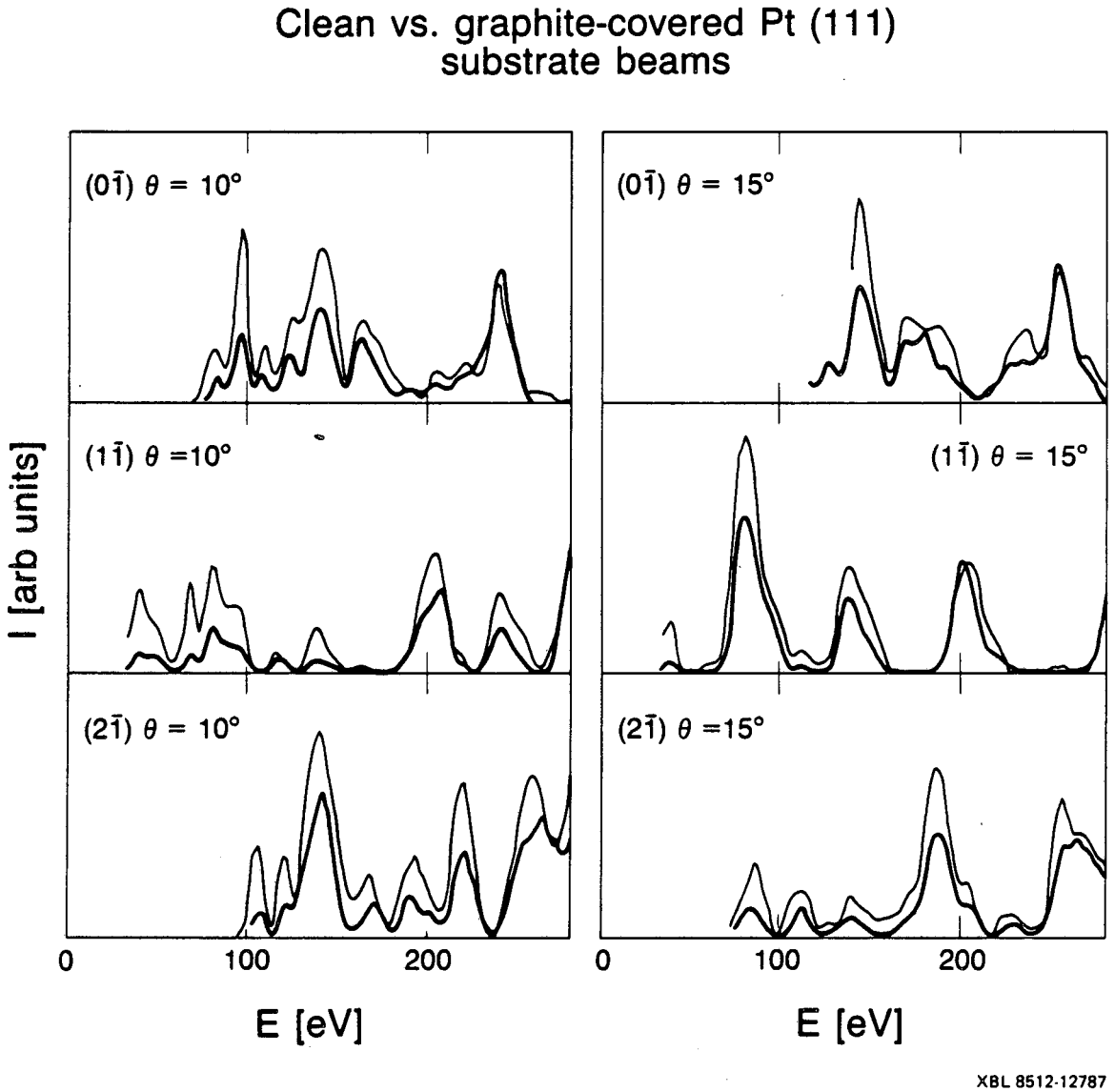
Clean vs. graphite-covered Pt (111)
substrate beams
(0$\bar{1}$) θ = 10°
(0$\bar{1}$) θ = 15°
(1$\bar{1}$) θ =10°
(1$\bar{1}$) θ = 15°
(2$\bar{1}$) θ = 10°
(2$\bar{1}$) θ =15°
I [arb units]
0
100
200
E [eV]
XBL 8512-12787

Fig. 5

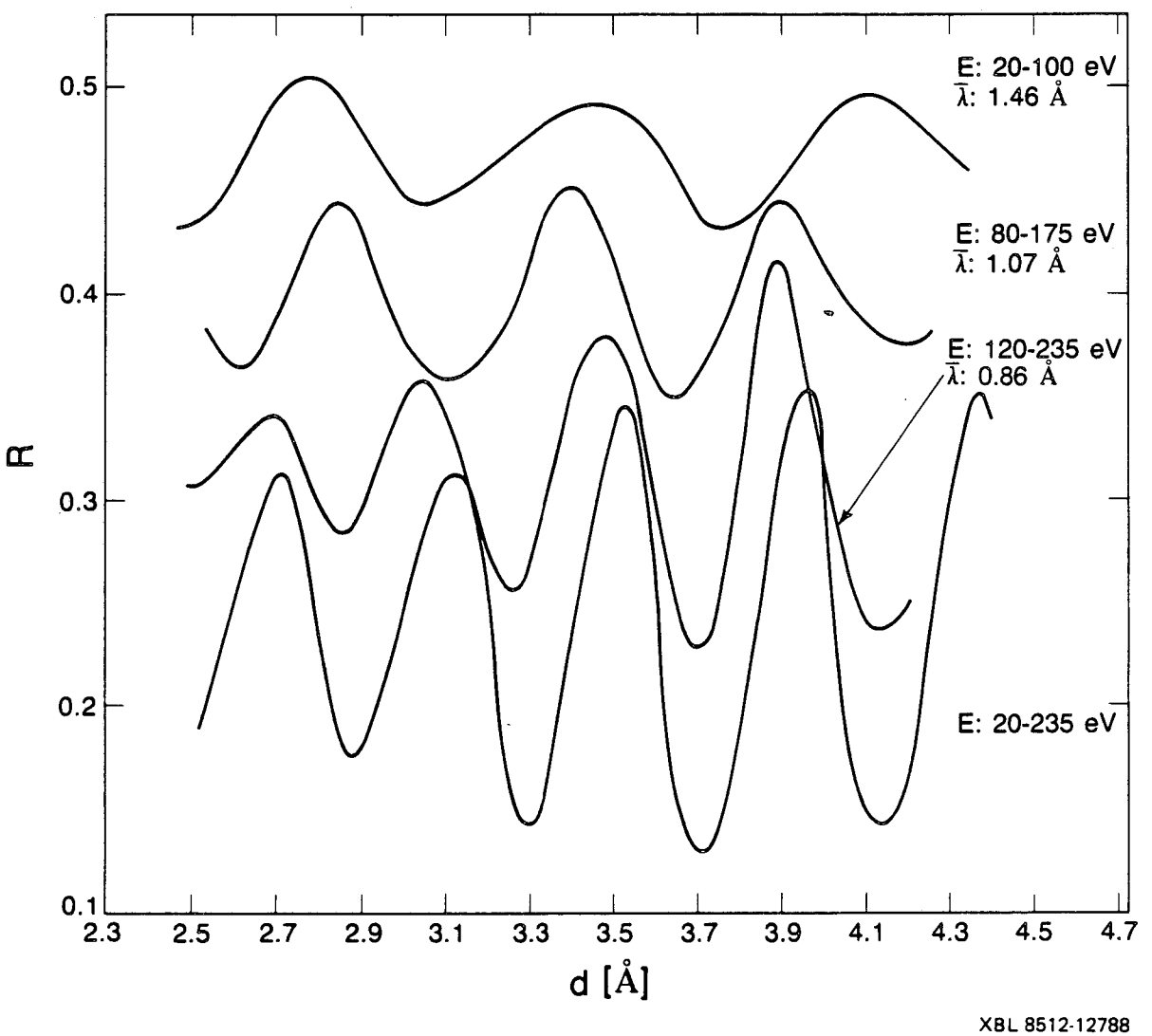
Graphite/Pt (111)
θ = 15°, φ = 150°, T = 300K
(00) beam
E: 20-100 eV
λ̄: 1.46 Å
E: 80-175 eV
λ̄: 1.07 Å
E: 120-235 eV
λ̄: 0.86 Å
E: 20-235 eV
R
d [Å]
0.5
0.4
0.3
0.2
0.1
2.3
2.5
2.7
2.9
3.1
3.3
3.5
3.7
3.9
4.1
4.3
4.5
4.7
XBL 8512-12788

Fig. 6

Graphite on Pt (111)
With and without C intercalate
θ = 15°, φ = 150°, T = 300K
(00) beam

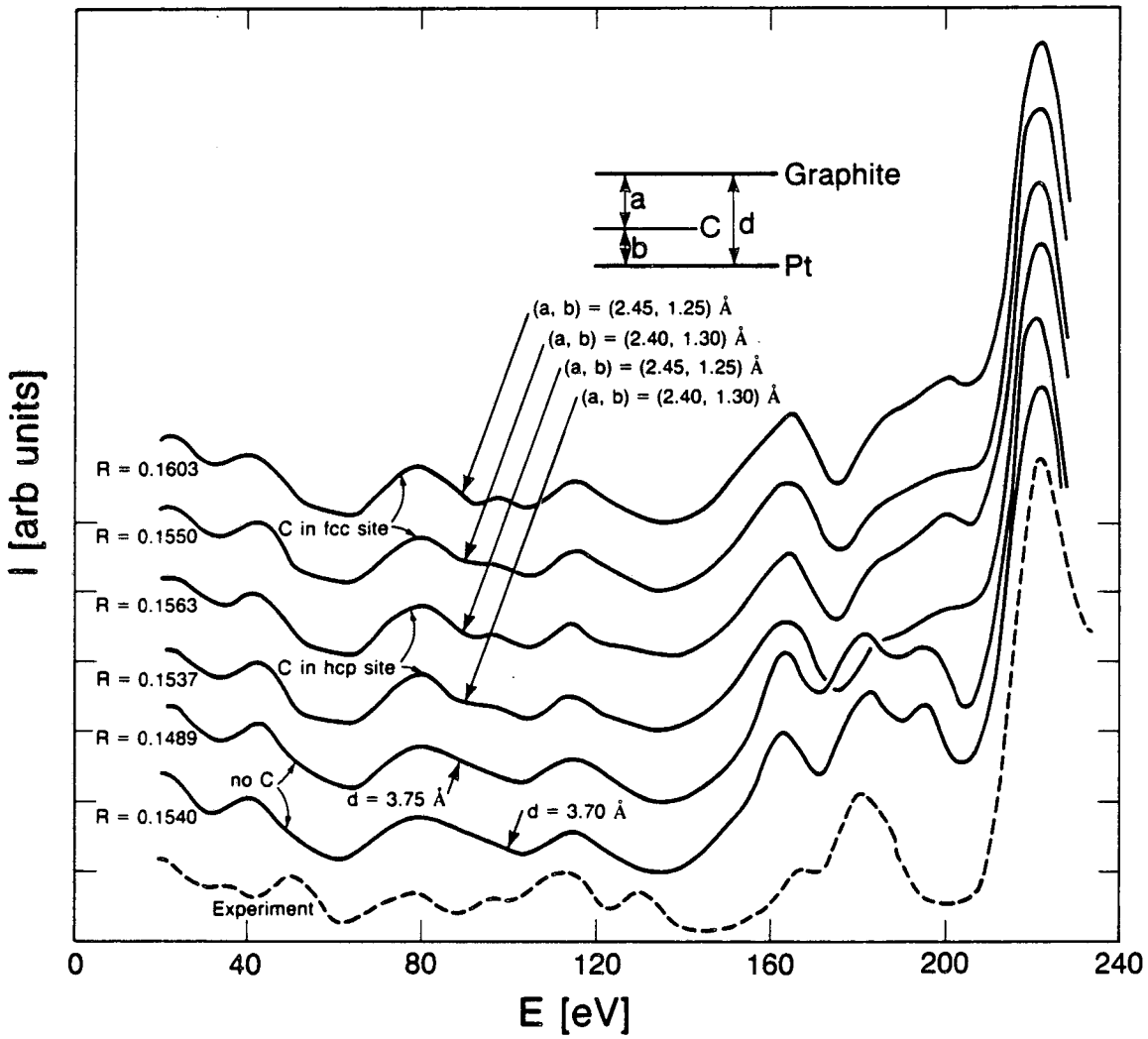

XBL 8512-12789

Fig. 7

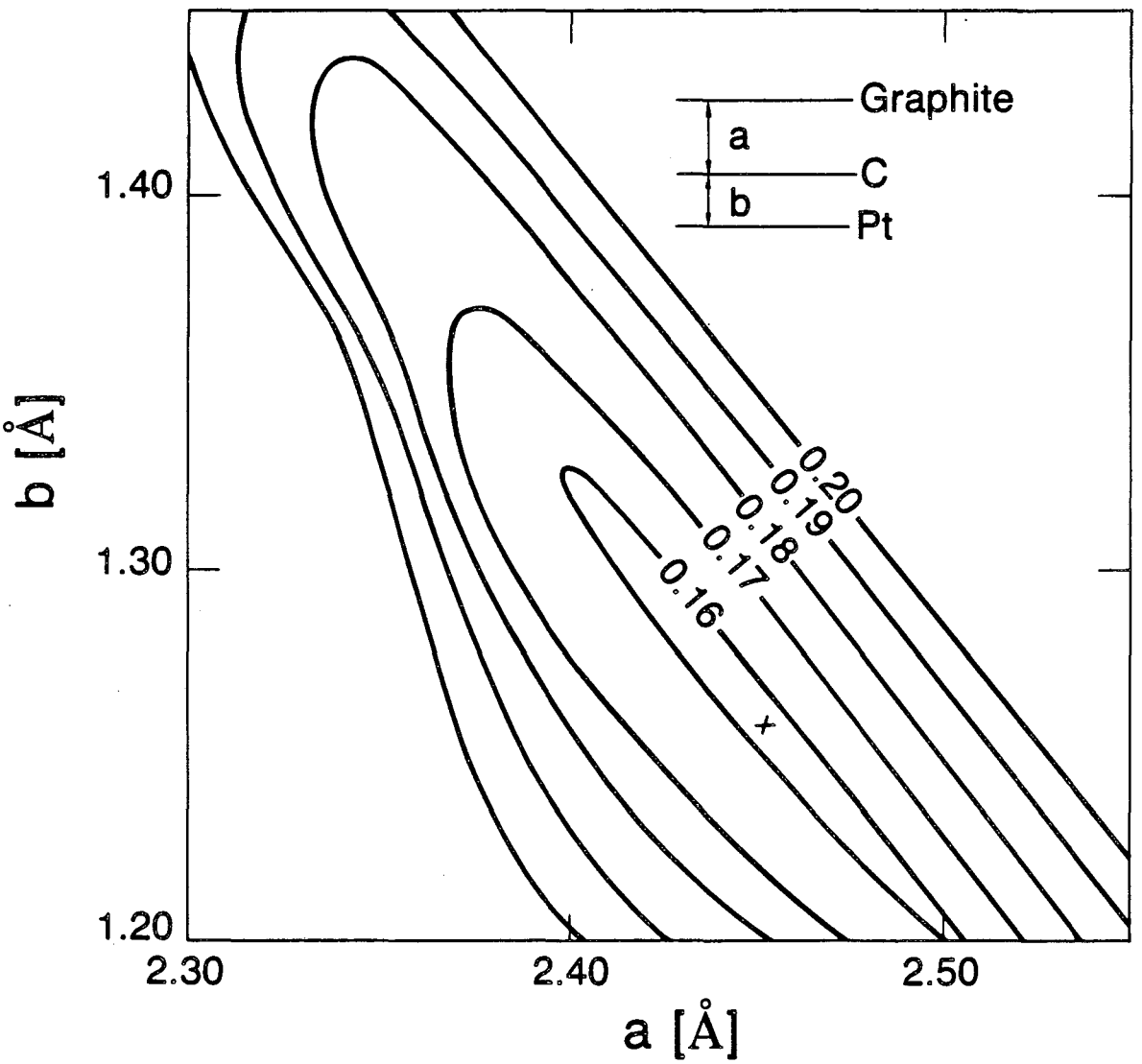
Graphite/C/Pt (111)
R-factor plot
(00) beam θ = 15°, φ = 150°
Graphite
a
C
b
Pt
0.20
0.19
0.18
0.17
0.16
1.40
1.30
1.20
2.30
2.40
2.50
b [Å]
a [Å]
XBL 8512-12791

Fig. 8

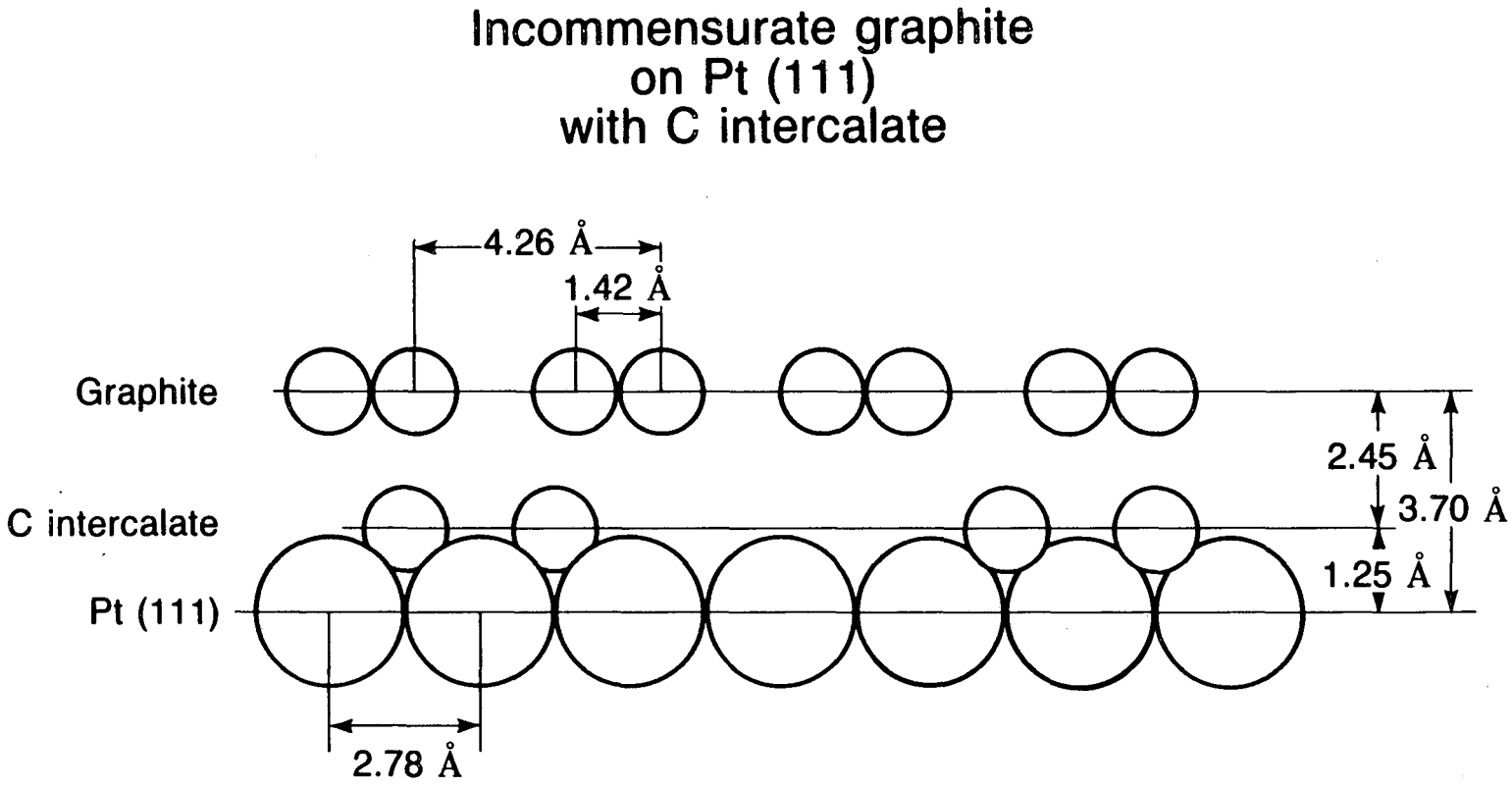
Incommensurate graphite
on Pt (111)
with C intercalate
4.26 Å
1.42 Å
Graphite
C intercalate
Pt (111)
2.45 Å
3.70 Å
1.25 Å
2.78 Å
XBL 8512-12785

Fig. 9

LAWRENCE BERKELEY LABORATORY
TECHNICAL INFORMATION DEPARTMENT
UNIVERSITY OF CALIFORNIA
BERKELEY, CALIFORNIA 94720